New Journal of Physics
The open access journal at the forefront of physics

Deutsche Physikalische Gesellschaft DPG IOP Institute of Physics

PAPER • OPEN ACCESS

Time-resolved x-ray phase-contrast tomography of sedimenting micro-spheres

To cite this article: A Ruhlandt and T Salditt 2019 *New J. Phys.* **21** 043017

New Journal of Physics
The open access journal at the forefront of physics

Deutsche Physikalische Gesellschaft DPG
IOP Institute of Physics

Published in partnership with: Deutsche Physikalische Gesellschaft and the Institute of Physics

OPEN ACCESS

RECEIVED
8 December 2018

REVISED
10 March 2019

ACCEPTED FOR PUBLICATION
27 March 2019

PUBLISHED
12 April 2019

PAPER

Time-resolved x-ray phase-contrast tomography of sedimenting micro-spheres

A Ruhlandt and T Salditt

Institut für Röntgenphysik, Georg-August-Universität Göttingen, Friedrich-Hund-Platz 1, Göttingen, Germany

E-mail: tsalditt@gwdg.de

Keywords: sedimentation, diffusion, phase contrast x-ray tomography, dynamic x-ray tomography

Supplementary material for this article is available online

Abstract

We have implemented a time-dependent (dynamic) x-ray tomography of sedimenting micro-spheres suspended in water. To achieve phase contrast at high magnification we use the divergent and highly coherent beam emitted from an x-ray waveguide. Holograms are recorded with 5 ms acquisition time while the sample is rotated at 1 Hz, over a run of 40 s. We show that under these conditions, more than 20 000 individual particle trajectories can be tracked. The analysis of the trajectories shows apparent super-diffusive behavior due to collective flow patterns, as also further evidenced by plotting the temporal averaged spatial distribution of particle densities and velocities.

Sedimentation is known as an important process in geology and biology, and is also one of the oldest technical processes to separate particles from liquids. Sedimentation is also of significant relevance for many modern techniques, from (ultra)-centrifugation, pharmaceutical formulation, to process engineering, including purification and controlled fabrication of deposits. On an industrial scale, processing of paper and pulp, paints, water purification, combustion and erosion, all involve sedimentation processes. From the point of view of soft condensed matter physics, colloidal sedimentation, as first investigated by J Perrin, remains fascinating, even if well studied [1, 2]. Interesting non-equilibrium effects such as shock-like fronts [3], stratification [4], and colloidal crystallisation kinetics [5] can be observed in sedimentation [6], and velocity correlations due to the long-range hydrodynamical interactions of the particles are of particular relevance [7, 8]. Despite its long history as a research field, many aspects of sedimentation remain poorly understood, in particular for the case of intermediate Péclet number $Pe \simeq 1$, where neither Brownian motion nor external driving forces can be neglected, and the processes are intrinsically non-stationary [9]. Even in simple model system of identical spherical particles settling in some container, surprising effects can occur such as colloidal inflations and settling disasters [10] or velocity fluctuations reminiscent of turbulence, despite the low Reynolds number [8].

For studies of colloidal sedimentation, scattering methods such as dynamic light scattering (DLS) or dynamic ultrasound provide valuable statistical information averaged over a large ensemble. This includes in particular the variance of particle velocity. X-ray photon correlation spectroscopy (XPCS) [11] access higher spatial frequencies than DLS, and can overcome the constraints associated with optical index-matching, which is required in optical techniques to prevent multiple scattering. XPCS can also access the regime of small Péclet numbers [12]. However, sedimentation cannot be completely described based on ensemble information of scattering methods. As a complementary approach, dynamics can be probed at the level of individual trajectories by microscopic techniques [13]. This allows in particular to access hydrodynamic velocity correlations between particles [14]. To this end, visible light microscopy and in particular confocal microscopy studies of fluorescently labelled particles are indispensable, but can easily run into problems for dense and strongly scattering suspensions. A major experimental challenge is therefore to achieve sufficient spatial and temporal resolution, even in dense and often non-transparent environments, for example in strongly scattering suspension in aqueous solution. Different optical techniques and the complementary nature of scattering and microscopic techniques are discussed in the review by [15].

Time-resolved (dynamic) x-ray computed tomography is in principle well suited to unravel slow dynamics of colloidal systems and more generally soft condensed matter in real space, if high spatial resolution in 3d can be combined with at least moderate temporal resolution. Novel experimental capabilities have been opened up by highly brilliant synchrotron sources, advanced x-ray optics, phase contrast, as well as faster detectors and progress in data processing. Indeed, a number of time-resolved tomography experiments have been reported for macroscopic objects, addressing the challenge that a dynamical object violates tomographic consistency. In fact, from simple alignment, to standard procedures such as filtered backprojection (FBP) to advanced algebraic reconstruction (ART, SIRT) and methods of iterative sinogram retrieval allowing for sparse sampling, internal motion in the object is usually primarily known as a source of artefacts. Correspondingly, tomography has to be generalized to non-stationary objects [16, 17]. To this end, prior knowledge about the object can be exploited to compensate for temporal and angular undersampling [18, 19], or optical flow can be analyzed to enhance backprojection by introduction of curved paths [20]. For mesoscopic and colloidal systems, however, this comes with the additional challenge of increased spatial resolution, in this work down to effective voxel sizes of 35 nm, requiring focused x-ray radiation and cone-beam recordings at high magnification. The x-ray optics needed in this case introduce wavefront errors, which are difficult to separate from the image, in particular for short acquisition time, and without the ptychographic and multiple-plane measurements available for stationary objects [21, 22].

In this work, we present an experimental approach to study dynamics of colloidal systems in 3D, based on advanced waveguide optics, continuous rotation and image acquisition above 100 Hz, combined with phase retrieval and particle tracking. By use of x-ray waveguide (WG) illumination we achieve high magnification, sensitivity to small phase shifts and reduced wavefront aberrations, facilitating later particle tracking. By using advanced planar waveguide devices placed in the focal plane of an elliptical mirror system (KB-mirror), we were able to increase WG flux such that exposure times of 5 ms yielded sufficient signal. In a proof-of-principle experiment we then reconstruct more than 10^4 trajectories of sedimenting SiO_2 micro-spheres in a water-filled capillary at $Pe = 14$. To this end, we first estimate the errors caused by the quasi-static assumption of a sliding window FPB reconstruction, and show that for given experimental parameters, identical particles can easily be tracked already from an under-sampled set of projections, treated by FBP. We then analyze the statistical properties of the single-particle trajectories, as well as the collective flow properties of sedimentation, convection, and advection.

The time-resolved tomography of sedimenting micro-spheres was carried out using the GINIX endstation at the storage ring PETRA III/beamline P10 of DESY, Hamburg [23], as illustrated in figures 1(a), (b). The undulator beam was monochromatized by a Si(111) monochromator to 8keV ($\simeq$0.01% bandwidth) and was focused to a spot size of about 300 nm $\times$ 300 nm by a pair of Kirkpatrick–Baez mirrors (KB). A x-ray waveguide was placed in the focal spot for spatial and coherence filtering, providing a 'clean' spherical illumination wavefront for in-line holography by transmitting only a small number of modes [24]. To enable short acquisition times, a high transmission one-dimensional waveguide was used, consisting of a 120 nm deep and 0.8 mm long channel etched into silicon, and capped by wafer bonding [25], resulting in a waveguide flux of about 2.8×10^{10} photons s^{-1}. The sample capillary was placed about 20 cm behind the waveguide in the highly divergent exit beam, on a rotation stage (UPR-160, Physik Instrumente) with maximum rotation frequency of 1 Hz, as sketched in figure 1(a). A geometrically magnified phase-contrast image (hologram) is then obtained by self-interference of the wave by free-space propagation to the detection plane at approximately 5 m distance, where the intensity pattern is recorded by a 20 μm thick LuAG:Ce scintillator screen (CRYTUR, Prague), fibre-coupled to a sCMOS sensor (C12849-102U, Hamamatsu Photonics) with 6.5 μm pixel size and full frame of 2048 $\times$ 2048 pixels. The micro-spheres (Fluka Analytical) of radius $a = 2 \pm 0.2$ μm made of SiO_2 with density $\varrho_{SiO_2} \approx 2.0$ g cm^{-3} were suspended in water with an initial solid content of 5%, and kept in a glass square capillary made of borosilicate glass with an inner edge length of 50 μm and a wall thickness of 25 μm (VitroCom Inc.,product nr. 8505). By using a square capillary shape, the rotation angle is 'encoded' in the projection images for post-gating, making it possible to use high frame rate recordings (i.e. 142 fps) of the camera without communication overhead with motor controllers. To this end, the maximum diameter of $\sqrt{2} \cdot 50$ μm ≈ 71 μm was kept smaller than the detector field of view, to have a margin at the side of the capillary. In fact the data shown below was recorded at geometric magnification $M = 224$, yielding an effective pixel demagnification factor of 112 and effective pixel size of 116 nm in the sample plane, after 2 $\times$ 2 binning for fast detector readout. The exposure time was set to 5 ms and the repetition time was 7 ms corresponding to a frame rate of 142 FPS. Already because of the capillary rotation alone with frequency of 1 Hz, a particle at a maximum distance of 35 μm from the rotation axis (i.e. in the corner of the capillary) moves by about 1.1 μm during exposure time. This is, however, small enough to discern particles and to keep the blur at a tolerable level.

The particle motion within the capillary is dominated by the gravitational force $F_g = \Delta\varrho V_s g$ with $V_s = 4/3\pi a^3$ the volume of the glass sphere, g the gravitational acceleration, and $\Delta\varrho = \varrho_{SiO_2} - \varrho_{H_2O}$ the difference in density. F_g exceeds the highest centrifugal force $F_c = \Delta\varrho V_s r\omega^2$ in the capillary at a rotation speed

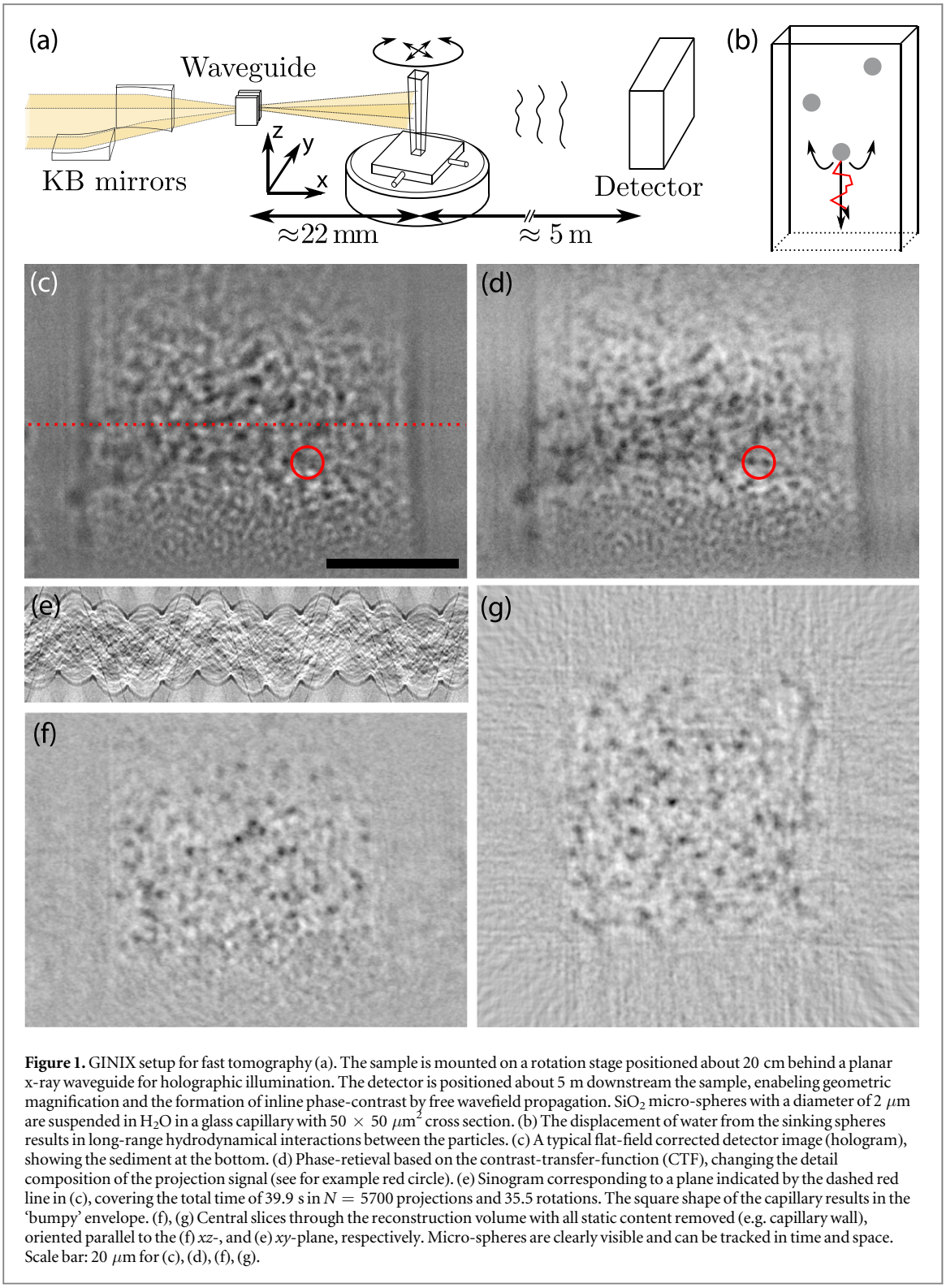

Figure 1. GINIX setup for fast tomography (a). The sample is mounted on a rotation stage positioned about 20 cm behind a planar x-ray waveguide for holographic illumination. The detector is positioned about 5 m downstream the sample, enabeling geometric magnification and the formation of inline phase-contrast by free wavefield propagation. SiO_2 micro-spheres with a diameter of 2 μm are suspended in H_2O in a glass capillary with 50 $\times$ 50 μm^2 cross section. (b) The displacement of water from the sinking spheres results in long-range hydrodynamical interactions between the particles. (c) A typical flat-field corrected detector image (hologram), showing the sediment at the bottom. (d) Phase-retieval based on the contrast-transfer-function (CTF), changing the detail composition of the projection signal (see for example red circle). (e) Sinogram corresponding to a plane indicated by the dashed red line in (c), covering the total time of 39.9 s in $N = 5700$ projections and 35.5 rotations. The square shape of the capillary results in the 'bumpy' envelope. (f), (g) Central slices through the reconstruction volume with all static content removed (e.g. capillary wall), oriented parallel to the (f) *xz*-, and (e) *xy*-plane, respectively. Micro-spheres are clearly visible and can be tracked in time and space. Scale bar: 20 μm for (c), (d), (f), (g).

of $\omega = 2\pi/\mathrm{s}$ by a factor of more than 4×10^4, allowing to neglect rotation-induced effects. In addition, the water column can be expected to follow the rotation without a noticeable delay, which is confirmed by inspection of the data. The time to reach a stationary rotation, i.e. until the water rotates with the capillary wall, is given by $t_{\mathrm{stat}} = d^2\rho_{H2O}/\eta$ [26], yielding $t_{\mathrm{stat}} \simeq 3.7$ ms for the present experimental values. Hence the stationary rotational flow is safely reached before the first exposure is recorded. Using STOKE'S law, the sedimentation speed of a single particle is evaluated to

$$v_s = \frac{2}{9}\frac{(\Delta\varrho)a^2 g}{\eta} \approx 2.2\ \mu\mathrm{m\ s}^{-1}, \tag{1}$$

resulting in a negligible motion of about 11 nm during the minimum exposure time. At the same time, Brownian motion for a diffusion constant $D = k_B T/(6\pi\eta a) \approx 0.215\ \mu\text{m}^2\ \text{s}^{-1}$ results in a mean displacement $\Delta r_t \approx \sqrt{6Dt}$ of about $\Delta r_{1\text{ s}} \approx 1.13\ \mu$m per second and $\Delta r_{5\text{ ms}} \approx 80$ nm during the exposure time. This meets the requirements of a discernable, but not too large displacement within the acquisition time of a sinogram. For given parameters, the Péclet number

$$Pe = a\frac{v_S}{D} \approx 10 \tag{2}$$

is in the regime where neither directed nor diffusive transport can be neglected. While these simple single particle relationships are appropriate to classify the regime of motion and optimize the experimental acquisition parameters, they of course ignore the more interesting hydrodynamic interactions between sedimenting beads and the walls. In particular, hydrodynamic backflow is expected in the closed chamber. Note that the experiment was started by turning a capillary with sedimented beads upside down, similar to turning an hourglass.

Figure 1(c) shows a representative projection image (hologram), recorded near the sediment (bottom), after dark- and flat-field corrections. For this run, 6975 images were recorded, including 5700 projections with constant maximum rotation speed, covering a process time of 39.9 s. The image shows patterns from sedimenting particles in the upper two thirds and a region of already sedimented spheres in the lower third (slowly rising throughout the acquisition by newly sedimented particles). The image in (c) exhibits the typical holographic appearance as expected for this regime of Fresnel number $F_1 \approx 0.002$ computed for a pixel demagnification of about 112 (after 2×2 rebinning), i.e. an effective pixel size of 116 nm. Phase-retrieval is exemplified in (d). It was carried out based on the (linearized) contrast transfer function (CTF), in which a regularized oscillatory Fourier filter is applied [27]. Although the overall impression changes only little, the composition of features shows decisive changes. This can be observed best in the highlighted areas. In the reconstruction (d) two dark spots appear within the red circle, whereas the signal is delocalized in the hologram (c). For single distance acquisition, CTF reconstruction suffers from pronounced artifacts. Further strong phase shifts such as in the sediment bed cannot be recovered. Figure 1(e) shows the sinogram corresponding to the plane indicated by the dashed line in (c). The following 3d reconstruction is additionally affected by motion artifacts and undersampling. At full rotation speed, 180° corresponding to a time lapse of 0.5 s are covered by 71 projections, well below the angular sampling criterion. However, given sparsity of micro-spheres allows for particle identification and tracking. Figures 1(f), (g) shows representative slices through the reconstruction volume, for orientations (f) along and (g) orthogonal to the rotation axis.

Using a sliding window of 0.5 s width, one 3d volume was reconstructed for every 0.125 s, resulting a total of 320 volumes covering the 39.9 s, enabling a threshold-based identification and subsequent motion tracking of the micro-spheres. To this end, the static parts were removed from all volumes by subtracting their temporal mean volume. In the next step, they were convolved with a model of an ideal sphere, smoothening the signal to remove outliers due to noise, motion- and phase-artifacts. The voxel with the highest signal in the volume was selected as the most probable position of a particle and symmetrically replaced by a zero valued sphere with twice the particle radius, since in this volume no second center of a bead can be expected. This maximum-searching and replacement procedure was repeated until a signal threshold was reached, resulting in a mean of about 4230 located candidates in each volume. The threshold was chosen by visual inspection such that the majority of spheres were correctly identified with only a small number of falsely recognized features. Such false positive positions are removed in the next step of tracking the particles. For this purpose, each position was connected to its nearest neighbor in the succeeding volume, provided the distance was smaller then a bead radius of 4 px. Gaps of one time step were closed by connecting trajectories with a distance of less than 6 px. The minimum accepted path length was 10 time steps, i.e. a particle present over the range of more than two full sinograms.

Figure 2 visualizes a selection of the 23 000 micro-sphere trajectories identified in the 4d dataset. The ten longest trajectories (each rendered in different color) are shown in panels (a–c), after projection to all three orthogonal planes. A histogram of identified trajectories against tracking duration is plotted in (d), showing that about 9000 trajectories are followed for a duration exceeding 10 s. The $N = 10, 100, 1000, 10^4$ longest trajectories are displayed in (e–h), respectively, illustrating the high density of trajectories within the capillary, see also supplemental material is available online at stacks.iop.org/NJP/21/043017/mmedia for a rendered movie of the particle trajectories. The majority of the trajectories display a fast sinking of the particles, but there are also segments with significant horizontal displacements and areas where spheres are ascending by advection. The identified single-particle trajectories can be analyzed in terms of the mean-square displacement (MSD) in the lateral (xy) plane. In the absence of hydrodynamic coupling one would expect a purely diffusive behavior. However, the MSD of the microspheres, as plotted in figure 3(a), exhibits super-diffusive characteristic, indicating the presence of currents in this plane. At the same time, the velocity auto-correlation of the trajectories shown in (b) decays rapidly to zero for the in-plane components $v_x(t)$ and $v_y(t)$, while the constant offset in the auto-correlation of $v_z(t)$ reflects the sedimentation.

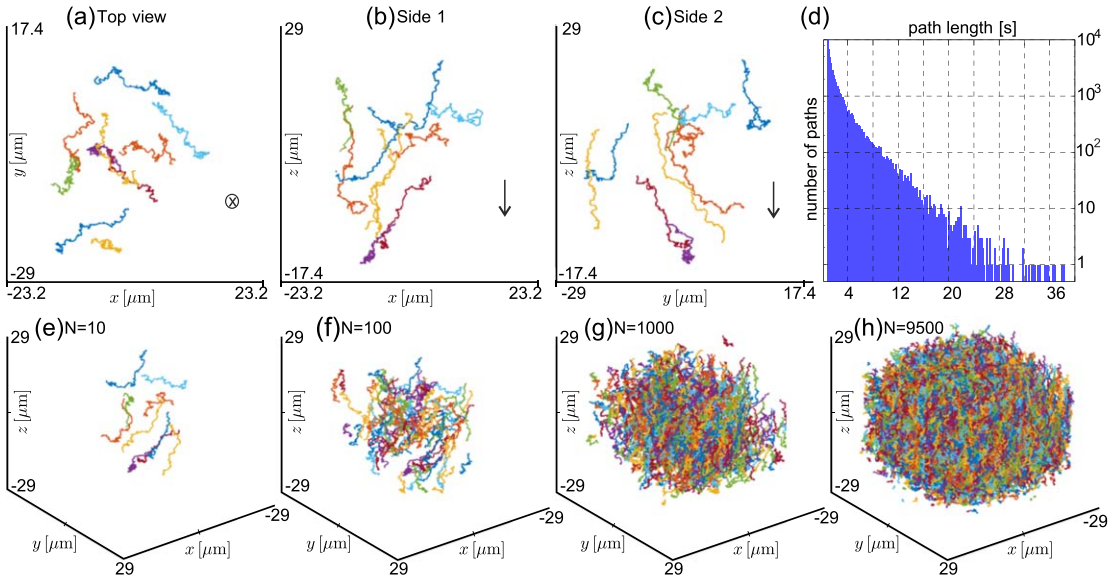

Figure 2. Trajectories of selected particles. (a)–(c) The ten longest reconstructed trajectories in the volume. Complex paths with large horizontal displacements and in some cases also ascending sections (advection) are observed. (d) A histogram of about 23 000 trajectories sorted as a function of path length. (e)–(h) 3d visualisation for the $N = 10, N = 100, N = 1000$, and $N = 9500$ longest trajectories, respectively.

Next, the collective flow and transport can be analyzed. First, the temporal mean particle density was calculated by averaging all detected positions of spheres over all time frames. To this end, each position of the 23 000 paths with a minimum length of 10 time frames, was represented by an ideal sphere. Projecting the volume of all spheres along one of the coordinate axes, we obtain the temporal mean fraction of solid content in the corresponding direction, as shown in the top row of figure 4. The *xz*-view in panel (a) shows a slightly higher particle density towards the bottom left quadrant. The high particle density in the lower part of the capillary seen in the side-views in panels (b), (c) corresponds to the zone just above the sedimenting front, where particles come to rest. Note that the actual solid sediment is not tracked. The spatial distribution of sedimentation speed is illustrated in figures 4(d)–(f), representing an average over time and one projection direction, orthogonal to the indicated plane displayed. To this end, each detected position of the 23 000 longest trajectories was represented by the ideal sphere weighted with the corresponding velocity in *z*-direction, and then projected along the selected direction. By division of the sphere density distribution, subjected to the same procedure, the local sedimentation velocity distribution can be plotted over the chosen plane. Clearly, a region of high sinking velocity (red) can be distinguished from a region of slowly rising particles (blue). The sinking spheres displace water which leads to upward flow and advection of spheres in neighboring areas, albeit with smaller advection than sedimentation velocity. In the lower half of the capillary, the velocities are smaller, the magnitude of the flow increases towards the top, as can be seen in the side view (e). This is illustrated further in panel (f), which displays *z*-averages of the top and bottom half of the 3d velocity distribution. Finally, the bottom row of figure 4 displays the temporal evolution of these sedimentation and advection currents in the top half of the capillary. The images show that a complex, slowly varying flow evolved during the measurement. This indicates the presence of convection/advection cells in the capillary, which are however, dominated by finite size effects and hydrodynamics coupling to the walls.

In summary, this proof-of-principle experiment provides a comprehensive insight into the 3d dynamics of the self-induced flows of sedimenting micro-spheres in the regime of moderate Péclet number and particle density. Geometrical magnification and free-space phase contrast have provided sufficient sensitivity to detect small sedimenting glass spheres suspended in water, even under the constraints of fast tomography and restricted angular sampling. For the present case, standard phase retrieval based on linearisation of optical functions and the CTF-formalism, and standard reconstruction based on FBP was sufficient, since neither the sediment floor with high phase shift, nor distortions in shape and phase shift of particles mattered for purpose of tracking. From the reconstructed single-particle trajectories, the 3d dynamics of the particles can be directly deduced at the level of single particles within a larger ensemble, including hydrodynamic interactions among particles and with walls. This is a significant improvement with respect to the prevailing x-ray scattering techniques which probe structure and dynamics (in the case of XPCS) in terms of averages over large ensembles. For the sedimentation problem considered here, we can learn how hydrodynamic interaction (in particular advection) leads to an apparently super-diffusive mean square displacement in the (lateral) plane normal to the

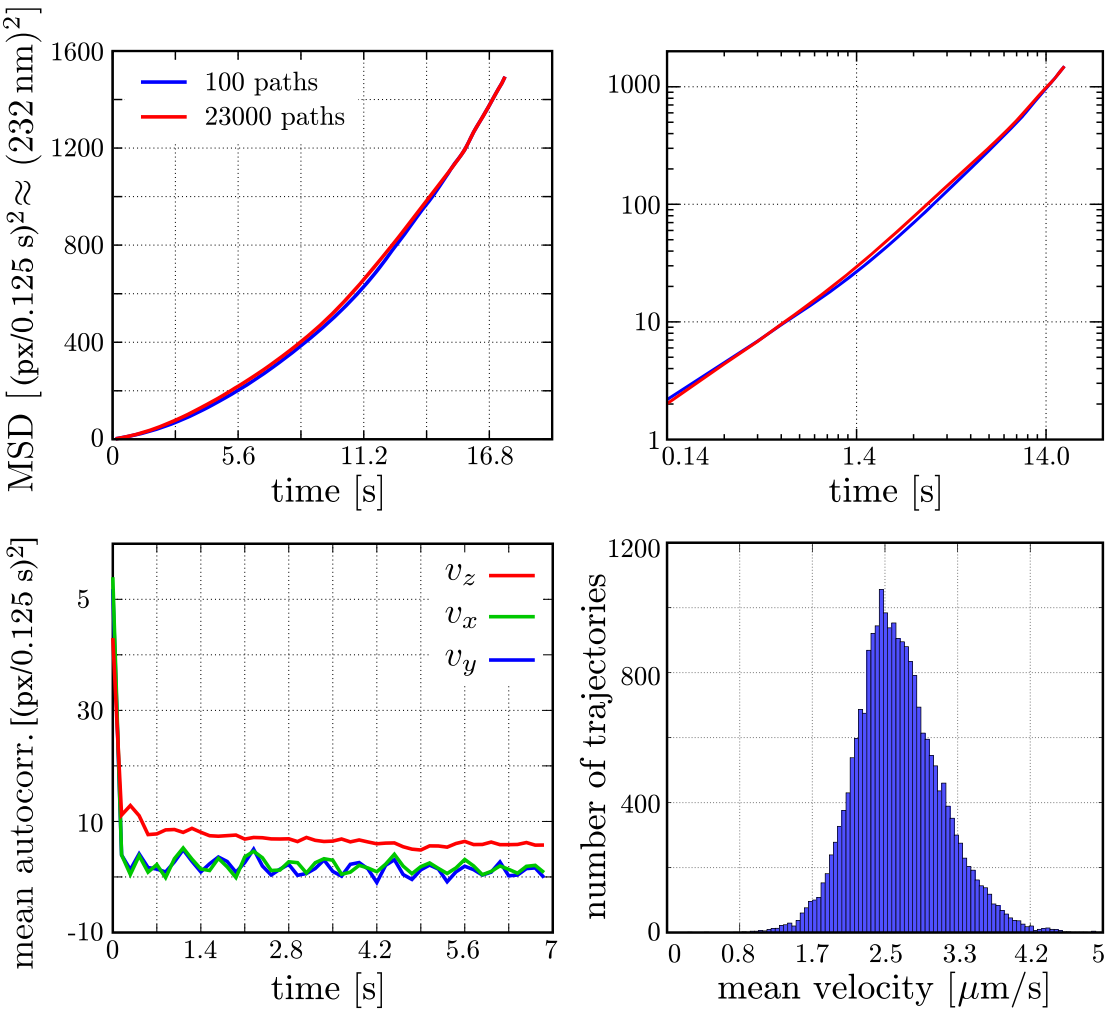

Figure 3. The mean squared displacement (MSD) of the particle trajectories (top row), velocity auto-correlation and velocity distribution (bottom row). (top left) MSD as a function of time in the lateral plane. A super-diffusive behavior is observed indicating transport by collective flow. The comparison of $N = 100$ and $N = 23\,000$ path proves consistence. (top right) Logarithmic plot of the MSD. (bottom left) Auto-correlation functions for the velocity components v_z, v_y, v_x averaged over the 150 longest paths. (bottom right) total velocity distribution with a mean of $v = 2.6\ \mu\text{m s}^{-1}$ and standard deviation $\sigma_v = 0.5\ \mu\text{m s}^{-1}$.

sedimentation axis (figure 3(a)). In other words we can quantify how vertical and lateral transport are coupled. The hydrodynamic flow pattern observed can be attributed to backflow and advection effects. Rayleigh-Bernard convection due to beam induced temperature gradients can be excluded, since the temperature gradients in the capillary by radiative heating do not reach the critical value.

Finally, we stress that the presented experimental approach is scalable and will profit from the ongoing and planned upgrades of many synchrotron facilities to a multi-bend achromat source. By using shorter exposure times, both the container size as well as the rotation speed could be increased without motional blur impairing the reconstruction quality. A higher rotation speed would then allow to investigate the dynamics of smaller sub-micron particles with higher diffusivity and smaller *Pe*, while a larger container minimizes the influence of boundary effects that dominate the flow dynamics in the present example. Rotational speed and container can be increased without risking a coupling between sedimentation and shear. The local heating by the beam, however, may become restrictive, when flux density has to be increased to compensate for shorter illumination time /faster rotation. For this reason, the sedimentation dynamics of small colloids is advantageously probed by scattering techniques. The applicability of dynamic tomography may be further extended, if prior knowledge of particle shape and composition as well as sparsity constraints could be better exploited in future reconstructions. This would make it possible to significantly under-sample rotational angles, in order to increase temporal resolution without more dose input. Furthermore, iterative phase retrieval could be used to reconstruct the solidification and crystallization of micro-beads and colloids at the sediment interface, which also is of significant fundamental interest.

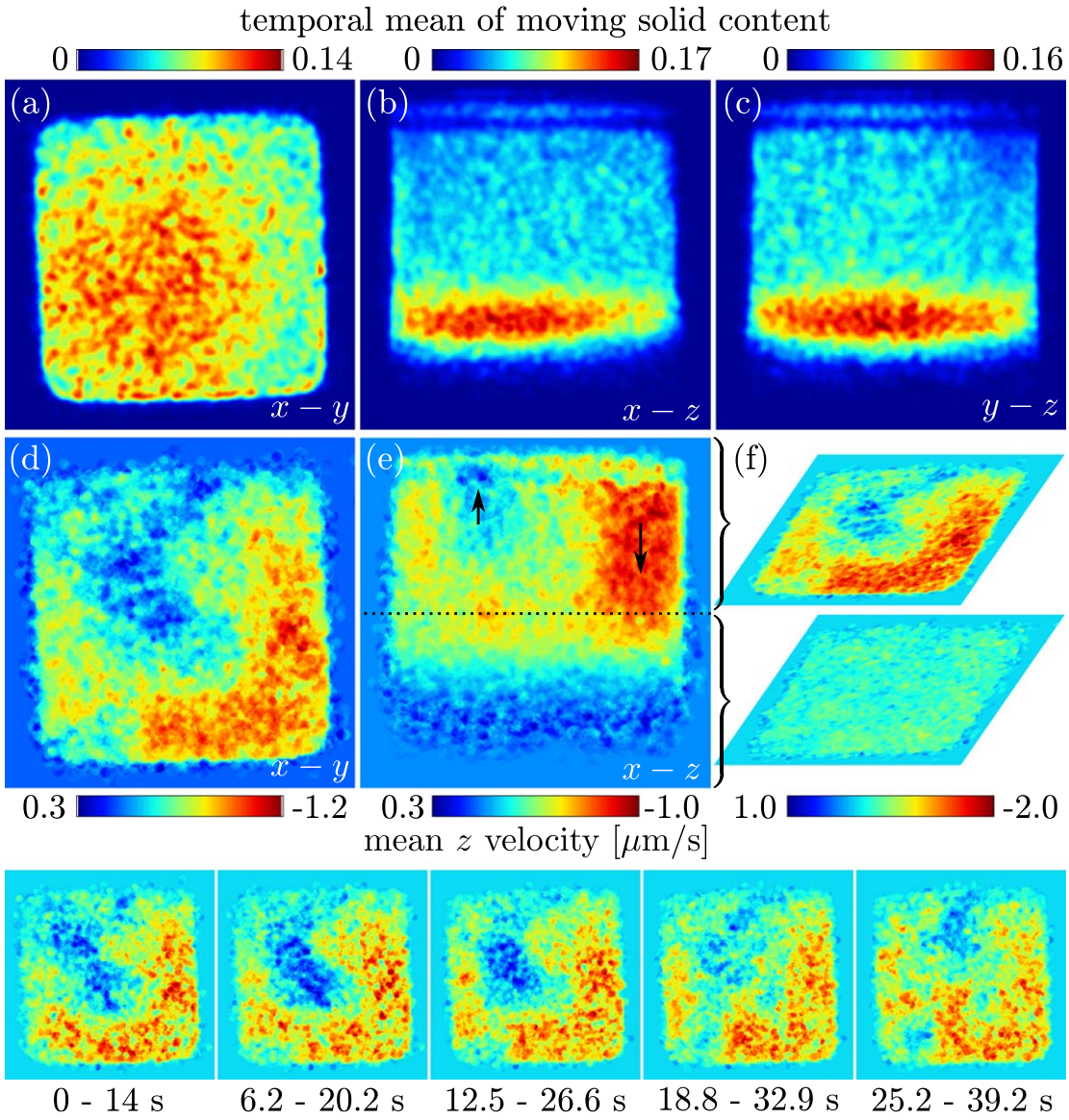

Figure 4. Temporal mean density of moving particles and collective dynamics in the capillary. Top row: (a) top and (b), (c) two side views of the mean density, after average along the third direction. Central row: (d) top and (e) side view (e) of the mean particle velocity component v_z. Regions of sinking spheres (red) can be clearly distinguished from regions of rising spheres (blue). (f) Velocity v_z averaged over the top and bottom half volume indicated in (e), indicating a slowing down of particles near the sediment interface. Bottom row: temporal evolution of the flow pattern in the top half, time-averaged over the indicated intervals. The colourbar of (f) applies also to the bottom row.

Acknowledgments

We thank Mareike Töpperwien, Malte Vassholz, and Markus Osterhoff for help with the experimental setup, and Michael Sprung for excellent working conditions at the P10 beamline, and acknowledge funding by SFB755/C1 *Nanoscale Photonic Imaging* of the German science foundation (DFG) as well as the German Ministry of Research (BMBF) through project 05K16MG2.

References

[1] Fernandez-Nieves A and Puertas A M (ed) 2016 *Fluids, Colloids and Soft Materials* (New York: Wiley)
[2] Bechinger C, Sciortino F and Ziherl P 2013 *Proc. Int. School of Physics 'Enrico Fermi'*
[3] Mills P and Snabre P 1994 *Europhys. Lett.* **25** 651–6
[4] Mueth D M, Crocker J C, Esipov S E and Grier D G 1996 *Phys. Rev. Lett.* **77** 578–81
[5] Palberg T 1999 *J. Phys.: Condens. Matter* **11** R323–60
[6] Löwen H 2001 *J. Phys.: Condens. Matter* **13** R415–32
[7] Segrè P N, Herbolzheimer E and Chaikin P M 1997 *Phys. Rev. Lett.* **79** 2574
[8] Segrè P N, Liu F, Umbanhowar P and Weitz D A 2001 *Nature* **409** 594
[9] Guzman-Sepulveda J E, Amin S, Lewis E N and Dogariu A 2015 *Langmuir* **31** 10351

[10] Piazza R, Buzzaccaro S and Secchi E 2012 *J. Phys.: Condens. Matter* **24** 284109
[11] Sandy A R, Zhang Q and Lurio L B 2018 *Annu. Rev. Mater. Res.* **48** 167–90
[12] Möller J and Narayanan T 2017 *Phys. Rev. Lett.* **118** 198001
[13] Nicolai H, Herzhaft B, Hinch E J, Oger L and Guazzelli E 1995 *Phys. Fluids* **7** 12
[14] Adnan H, Molina J and Ryoichi Y 2013 *Soft Matter* **9** 10056
[15] Palberg T 2014 *J. Phys. D: Condens. Matter* **26** 333101
[16] Bonnet S *et al* 2003 *Proc. IEEE* **91** 1574
[17] Walker S M *et al* 2014 *PLoS Biol.* **12** e1001823
[18] Gibbs J *et al* 2015 *Sci. Rep.* **5** 11824
[19] Kazantsev D *et al* 2016 *J. X-Ray Sci. Technol.* **24** 207
[20] Ruhlandt A, Töpperwien M, Krenkel M, Mokso R and Salditt T 2017 *Sci. Rep.* **7** 6487
[21] Robisch A L, Wallentin J, Pacureanu A, Cloetens P and Salditt T 2016 *Opt. Lett.* **41** 5519
[22] Hagemann J, Robisch A L, Osterhoff M and Salditt T 2017 *J. Synchrotron Radiat.* **24** 489
[23] Salditt T *et al* 2015 *J. Synchrotron Radiat.* **22** 867
[24] Bartels M, Krenkel M, Haber J, Wilke R N and Salditt T 2015 *Phys. Rev. Lett.* **114** 048103
[25] Hoffmann-Urlaub S, Höhne P, Kanbach M and Salditt T 2016 *Microelectron. Eng.* **164** 134
[26] Guyon E, Hulin J P and Petit L 1994 *Hydrodynamik* (Oxford: Oxford University Press)
[27] Cloetens P *et al* 1999 *Appl. Phys. Lett.* **75** 2912